



Partitioning of localized and diffuse deformation in the Tibetan Plateau from joint inversions of geologic and geodetic observations

J.P. Loveless*, B.J. Meade

Department of Earth and Planetary Sciences, Harvard University, 20 Oxford Street, Cambridge, MA 02138, USA

ARTICLE INFO

Article history:

Received 5 July 2010

Received in revised form 30 November 2010

Accepted 6 December 2010

Available online 22 January 2011

Editor: R.D. van der Hilst

Keywords:

Tibet
GPS
deformation
microplate
modeling
block model
Monte Carlo

ABSTRACT

The spatial complexity of continental deformation in the greater Tibetan Plateau region can be defined as the extent to which relative motion of the Indian and Asian plates is partitioned between localized slip on major faults and distributed deformation. Potency rates provide a quantitative metric for determining the magnitudes of diffuse and on-fault crustal deformation, which are proportional to strain rates within crustal micro-plates and fault slip rates, respectively. We simultaneously estimate micro-plate rotation rates, interseismic elastic strain accumulation, fault slip rates on major structures, and strain rates within 24 tectonic micro-plates inferred from active fault maps in the greater Tibetan Plateau region using quasi-static block models constrained by interseismic surface velocities at 731 GPS sites and 9 Holocene–Late Quaternary geologic fault slip rates. The joint geodetic–geologic inversion indicates that geologic slip rates are kinematically consistent with differential micro-plate motions. Estimated left-lateral slip rates on the Altyn Tagh, west-central Kunlun, and Xianshuihe faults are relatively homogeneous along strike (~11.5, 10.5, and 11 mm/yr, respectively) while segmentation of the eastern Kunlun fault by the intersecting Elashan and Riyueshan faults results in a decreased slip rate, consistent with geologic observations. The fraction, ϕ , of total potency rate associated with intrablock strain, uncorrected for observational noise, ranges from 0.27 in the Himalayan Range block to 0.91 in the Aksai Chin block. Monte Carlo simulations are used to quantify the likelihood that internal deformation is statistically distinguishable from the uncertainties in geodetic velocities. These simulations indicate that internal block deformation is statistically significant only within the Himalayan Range Front (where internal deformation accounts for $\phi_{ID} = 0.11$ of block potency rate budget), west-central plateau ($\phi_{ID} = 0.68$), Ganzi-Yushu/Xianshuihe (0.58), Burma (0.09), Jiali (0.38), and Aksai Chin (0.68) blocks. In the other 18 tectonic micro-plates within the plateau region, estimated internal block potency is not currently distinguishable from the expected contribution of observational noise to residual velocities. Of the total potency budget within the Tibetan Plateau, 85% is taken up by slip on major faults, with the remaining 15% accommodated by internal processes at sub-block scale distinguishable from observational noise. The localization of the majority of plate boundary activity is also supported by the spatial distribution of modern and historical crustal earthquakes. Sixty-seven percent of the total moment released by earthquakes in the CMT catalog and 90% of historical moment since 1900 have been released within 25 km of the major faults included in the block model, representing only 12% of the characteristic half-block length scale of ~215 km. The localization of deformation inferred from geologic, geodetic, and seismic observations suggests that forces applied to tectonic micro-plates drive fault system activity at the India–Asia collision zone over decadal to Quaternary time scales.

© 2010 Elsevier B.V. All rights reserved.

1. Introduction

Deformation at active continental plate boundaries has been approximated using the micro-plate and continuum end-member hypotheses. The former assumes that the majority of deformation is localized on an effectively countable number of major faults forming the boundaries of tectonic micro-plates (e.g., [Avouac and Tapponnier, 1993](#); [Meade, 2007](#); [Shen et al., 2005](#); [Thatcher, 2007](#)), while the latter (e.g.,

[England and Molnar, 2005](#); [Flesch et al., 2001](#); [Molnar, 1988](#)) approximates the kinematics of continental deformation as diffusely distributed across active plate boundaries. The two concepts are linked by the idea that as more faults are introduced, individual micro-plate sizes decrease and, if fault slip rates become more homogeneous, the bulk behavior of a micro-plate system might approach the predictions of the continuum approximation (e.g., [Thatcher, 2003, 2009](#)). Debate about the adequacy of the two end-member approximations has been focused on the Tibetan Plateau ([Avouac and Tapponnier, 1993](#); [England and Molnar, 2005](#); [Jade et al., 2004](#); [Meade, 2007](#); [Molnar, 1988](#); [Thatcher, 2007](#); [Zhang et al., 2004](#)), which deforms to accommodate the relative motion between the Indian and Asian plates. Recent field-based

* Corresponding author.

E-mail address: loveless@eps.harvard.edu (J.P. Loveless).

investigations of slip rates on the Altyn Tagh fault have suggested upper crustal behavior that shows both strong localization on identifiable faults and an unquantified amount of distributed deformation across wider shear zones (Cowgill et al., 2009). At a regional scale, wide aperture geodetic networks provide decadal surface velocity estimates that can contribute to the determination of where on the spectrum between the two end-member deformation models present-day crustal activity lies. Global Positioning System (GPS) velocity fields in Tibet have been acquired through the interseismic phase of the earthquake cycle to avoid including the displacements from large earthquakes (Gan et al., 2007; Wang et al., 2001; Zhang et al., 2004). During the interseismic phase of the seismic cycle, elastic strain accumulation produces smoothly varying geodetic velocities near faults (e.g., Savage and Burford, 1973), which may be detectable at the 1 mm/yr level as far as 500 km from the Himalayan Range Front and 100–150 km from other active faults in Tibet (Bilham et al., 1997; Feldl and Bilham, 2006; Hilley et al., 2005). Because of the smooth velocity gradient across faults, as well as sparse geologic slip rate constraints on the most active faults in Tibet, GPS data have been interpreted either as reflecting diffuse deformation neglecting elastic strain accumulation (Jade et al., 2004; Zhang et al., 2004), or as consistent with block models that formally combine micro-plate rotations and earthquake cycle processes (Chen et al., 2004; Hilley et al., 2009; Meade, 2007).

Here we integrate the two end-member points of view, quantifying the spatial complexity of upper crustal deformation in Tibet using potency (geometric moment) rates to describe the partitioning of localized and diffuse strain. We simultaneously solve for micro-plate rotations, earthquake cycle effects, and internal block deformation with a quasi-static, three-dimensional block model (Fig. 1) constrained by both interseismic GPS velocities (Fig. 2) and geologic fault slip rates (Table 1; Fig. 3), allowing for analysis of recent deformation of the Tibetan Plateau region in a way that is consistent with decadal to Late Quaternary observations. Internal block strain rate estimates include a combination of unmodeled processes (e.g., minor faults and folding) and observational noise. In order to quantify the proportion

of the internal potency rate that is likely due to deformation, we estimate the contribution to the residuals from observational noise using Monte Carlo simulations. Estimates of internal potency rates define quantitative bounds on the partitioning of continental deformation in the Tibetan Plateau region that are tested against the spatial distribution of large earthquakes and moment release estimates from historical and instrumental catalogs.

2. Deformation partitioning analysis

For a given fault system geometry and set of geodetic and geologic observations, the partitioning of localized and diffuse deformation can be determined from a comparison of potency rates, quantifying the magnitude of deformation associated with each. The potency rate accommodated by major faults included in the block model, P_f , is given by the product of fault area, A , and slip rate magnitude, $|s|$: $P_f = A|s|$ (e.g., Aki and Richards, 1980). The potency rate associated with deformation occurring within crustal micro-plates, P_b , can be derived from Kostrov's moment summation approach (Kostrov and Das, 1988) as twice the product of the internal block strain rate magnitude, $|\epsilon|$, and the block volume, V_b : $P_b = 2V_b|\epsilon|$. Given P_f and P_b for each micro-plate, we calculate the potency rate partitioning value, ϕ , as

$$\phi = \frac{P_b}{P_f + P_b}. \quad (1)$$

In the limiting case where all deformation is localized as slip on faults included in a model, $P_b = 0$ and $\phi = 0$. Conversely, if no deformation occurs on the included faults and internal micro-plate strain accounts for all potency, $P_f = 0$ and $\phi = 1$. The quantity ϕ may be applied to any kinematic model of crustal motions to evaluate the partitioning of localized and diffuse deformation.

Both localized and diffuse potency rates can be determined from a joint block model analysis of geodetic and geologic data. Block models

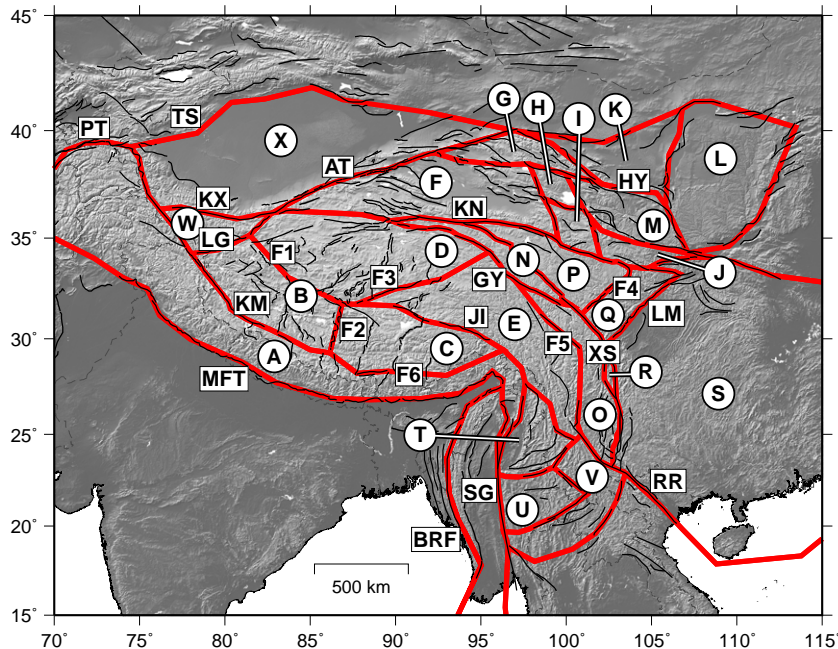


Fig. 1. Active faults (black lines; Taylor and Yin, 2009) and reference model block geometry (red lines, with blocks identified by circled letters). Major faults labeled are the Main Frontal Thrust (MFT), Karakorum (KM), Longmu-Gozha (LG), Karakax (KX), Pamir Thrust (PT), Tien Shan range front (TS), Altyn Tagh (AT), Jiali (JI), Ganzi-Yushu (GY), Burman Range Front (BRF), Sagaing (SG), Red River (RR), Xianshuihe (XS), Longmenshan range front (LM), Kunlun (KN), and Haiyuan (HY); unnamed faults are F1–F6. The blocks are labeled as: Himalayan Range (A), Karakorum (B), Jiali (C), west-central plateau (D), east-central plateau (E), Qaidam Basin (F), Qilian Shan (G), Elashan (H), Gonghe Nan Shan (I), West Qinling (J), Haiyuan (K), Ordos Plateau (L), Lanzhou (M), Ganzi-Xianshuihe sliver (N), Lugu Lake (O), eastern Kunlun (P), Longmenshan (Q), Anninghe-Daliangshan sliver (R), south China (S), Yunnan (T), Burma (U), Laos (V), Aksai Chin (W), and Tarim Basin (X).

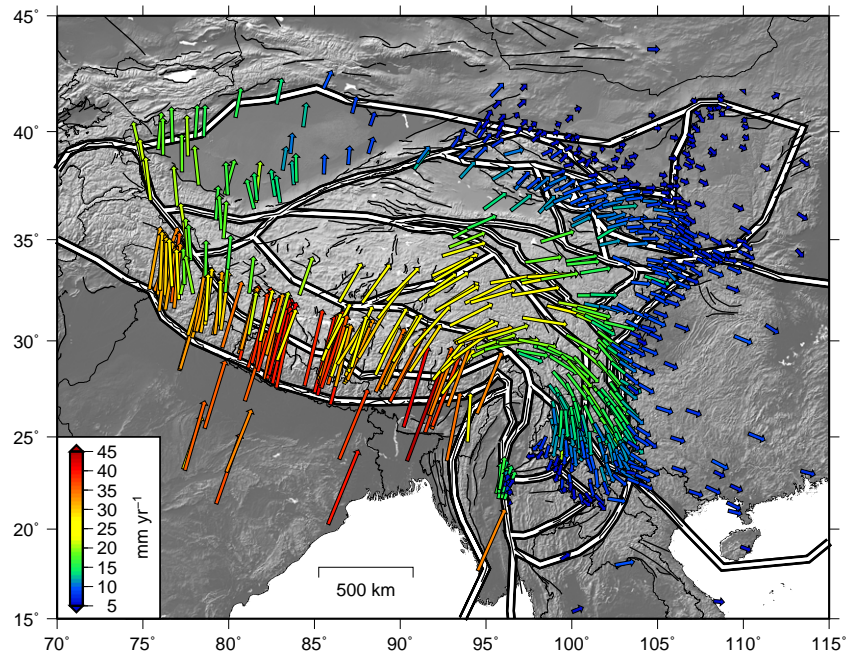


Fig. 2. Nominally interseismic GPS velocities expressed relative to a stable Eurasian reference frame. We combined the velocity fields of [Apel et al. \(2006\)](#), [Banerjee et al. \(2008\)](#), [Calais et al. \(2006\)](#), [Gan et al. \(2007\)](#), and [Vigny et al. \(2003\)](#) into a common reference frame by finding rotation and translation parameters that minimize the difference between velocities at collocated stations. Velocities are listed in Table A1.

combine the assumption that fault slip rates result from differential micro-plate rotations with quasi-static earthquake cycle models to estimate fault slip rates and micro-plate rotation vectors using observations of interseismic deformation (e.g., [Bennett et al., 1996](#); [Matsu'ura et al., 1986](#); [McCaffrey, 2002](#); [Meade and Hager, 2005](#); [Meade and Loveless, 2009](#); [Murray and Segall, 2001](#); [Prawirodirdjo et al., 1997](#); [Souter, 1998](#)). The linear forward problem can be written as $\mathbf{G}\mathbf{m}=\mathbf{d}$, where $\mathbf{d}=[\mathbf{v} \ \mathbf{s}_g]^T$ is a vector comprising the nominally interseismic, geodetically observed surface velocity field, \mathbf{v} , and a set of geologically constrained fault slip rates, \mathbf{s}_g ; \mathbf{m} is a vector of Cartesian rotation vector components for all crustal micro-plates; and \mathbf{G} is the Jacobian relating surface velocities and slip rate constraints to micro-plate rotation vectors and interseismic earthquake cycle deformation near locked (e.g., [Savage and Burford, 1973](#)), finite length ([Okada, 1985](#)), block-bounding faults ([Matsu'ura et al., 1986](#)). The estimated coupled micro-plate rotation vectors, $\hat{\mathbf{m}}$, are found using a weighted least-squares inversion, $\hat{\mathbf{m}}=(\mathbf{G}^T\mathbf{W}\mathbf{G})^{-1}\mathbf{G}^T\mathbf{W}\mathbf{d}$, where \mathbf{W} is a diagonal data weighting matrix with non-zero entries proportional to the inverse square of the reported geodetic velocity

and geologic slip rate uncertainties. Kinematically consistent slip rate estimates, $\hat{\mathbf{s}}$, are determined by projecting the rotation vectors, $\hat{\mathbf{m}}$, describing relative micro-plate motions onto the three-dimensional fault system geometry.

Fault slip rates and geometry provide the information necessary to calculate the on-fault potency rate, P_f , for each block,

$$P_f = \sum_{k=1}^{N_f} \frac{|\mathbf{s}^{(k)}| L^{(k)} D^{(k)}}{2 \sin \delta^{(k)}}, \quad (2)$$

where $|\mathbf{s}^{(k)}|$ is the magnitude of the estimated slip rate for fault segment k , $L^{(k)}$ is the segment length, $D^{(k)}$ is the segment locking depth, $\delta^{(k)}$ is the segment dip, and the summation is made over all N_f segments that bound the block. The division by 2 is required so that half of the fault slip rate is counted for each of the two blocks that the fault segment bounds when calculating potency rates.

To calculate internal block strain rates with no assumption about strain coherence, we use the set of estimated micro-plate rotation

Table 1
Geologic slip rate constraints used in the joint inversion block model.

Fault name ^a	Sense ^b	Slip rates (mm/yr)			Age (ka) ^e	Source
		Reported	Estimated ^c	Estimated ^d		
a. Karakorum	RL	4.0 ± 1.0	4.0 ± 0.1	4.0 ± 0.6	11–14	Brown et al. (2002)
b. Altyn Tagh	LL	11.7 ± 1.6	11.2 ± 0.2	8.3 ± 0.6	6.4	Cowgill (2007)
c. Kunlun	LL	10.0 ± 1.5	10.0 ± 0.1	13.1 ± 0.6	6	Haibing et al., (2005)
d. Kunlun	LL	10.9 ± 0.5	10.8 ± 0.0	8.7 ± 0.5	5.6–11	Van der Woerd et al. (2002)
e. Kunlun	LL	5.0 ± 0.4	5.0 ± 0.0	6.7 ± 0.7	12.6	Kirby et al. (2007)
f. Kunlun	LL	2.0 ± 0.4	2.0 ± 0.0	4.7 ± 0.6	9.1	Kirby et al. (2007)
g. Haiyuan	LL	4.5 ± 1.1	4.6 ± 0.1	6.2 ± 0.5	3.2–13.7	Li et al. (2009)
h. Ganzi–Yushu	LL	12.0 ± 2.0	11.7 ± 0.2	5.6 ± 0.5	50	Wen et al. (2003)
i. Main Frontal	RV	21.0 ± 1.5	20.9 ± 0.1	20.7 ± 0.3	2.2–9.7	Lavé and Avouac (2000)

^a Constrained segments are identified in [Fig. 3](#).

^b RL = right-lateral, LL = left-lateral, RV = reverse.

^c Joint inversion.

^d Geodetic-only inversion.

^e Age of timing constraints.

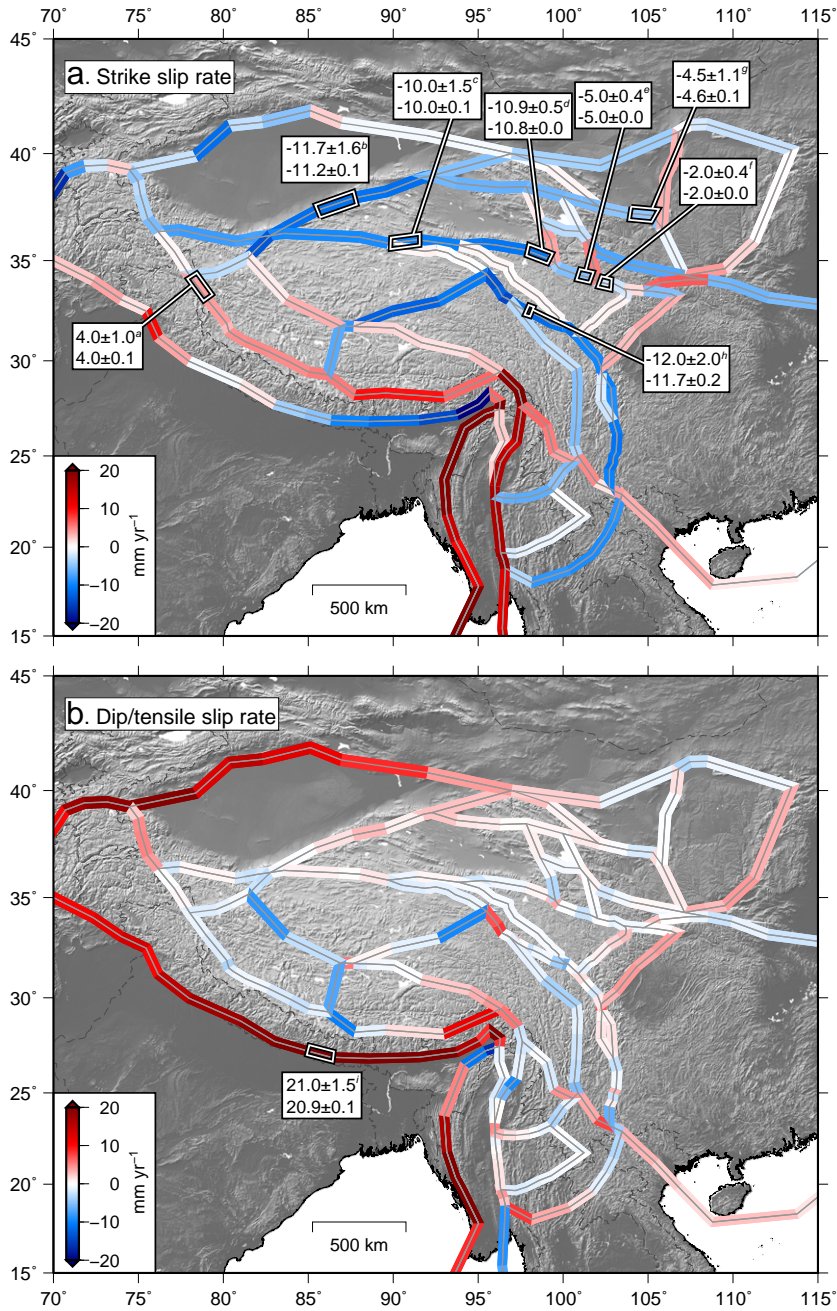


Fig. 3. Estimated a) strike and b) dip/tensile fault slip rates from the combined geodetic–geologic block model inversion. Right-lateral and reverse/closing sense slip are given as positive. Outlined fault segments indicate locations of geologic slip rate constraints, with the label giving the input (top) and estimated (bottom) rates and uncertainties. Superscripts give source of slip rate constraint: ^aBrown et al. (2002); ^bCowgill (2007); ^cHaibing et al. (2005); ^dVan der Woerd et al. (2002); ^eKirby et al. (2007); ^fLi et al. (2009); ^hWen et al. (2003); ⁱLavé and Avouac (2000).

vectors and the Jacobian to calculate the predicted data vector, $\mathbf{G}\hat{\mathbf{m}} = [\hat{\mathbf{v}} \hat{\mathbf{s}}_g]^T$, where $\hat{\mathbf{v}}$ is the predicted velocity field and $\hat{\mathbf{s}}_g$ are the slip rate estimates on the geologically constrained segments. We carry out a Delaunay triangulation of GPS stations within each crustal block and, for each triangle, calculate the horizontal displacement rate gradient tensor, \mathbf{D} , of the residual velocity field, $\hat{\mathbf{r}} = \mathbf{v} - \hat{\mathbf{v}}$ (Fig. 4a), with components $D_{ij} = \partial \hat{r}_i / \partial x_j$, where \hat{r}_i is the residual velocity in the i direction and x_j is the station coordinate in the j direction. We discard triangular elements whose edges intersect block boundaries, yielding a set of elements entirely internal to each block. We assume that \mathbf{D} is constant throughout each element (Fig. 4b) and decompose \mathbf{D} into a symmetric strain rate tensor, ϵ , and antisymmetric rotation rate tensor, ω , and use the strain rate magnitude, $|\epsilon|$, and volumes of

the triangular prisms, V_t (triangular elements at the surface extruded to a depth equivalent to the estimated block-bounding fault locking depth), to calculate the potency rate, $P_t = 2V_t|\epsilon|$. We calculate the total potency rate within each block, P_b , by summing the P_t values for all N_t triangular prisms, scaling the contribution of each prism by its volume relative to the total volume of the tessellation prism, V_T , and multiplying by the block volume, V_b , given as the area inscribed by all block fault segments extruded to the fault locking depth and accounting for non-vertical fault dips,

$$P_b = V_b \sum_{k=1}^{N_t} \frac{P_t^{(k)}}{V_T}. \quad (3)$$

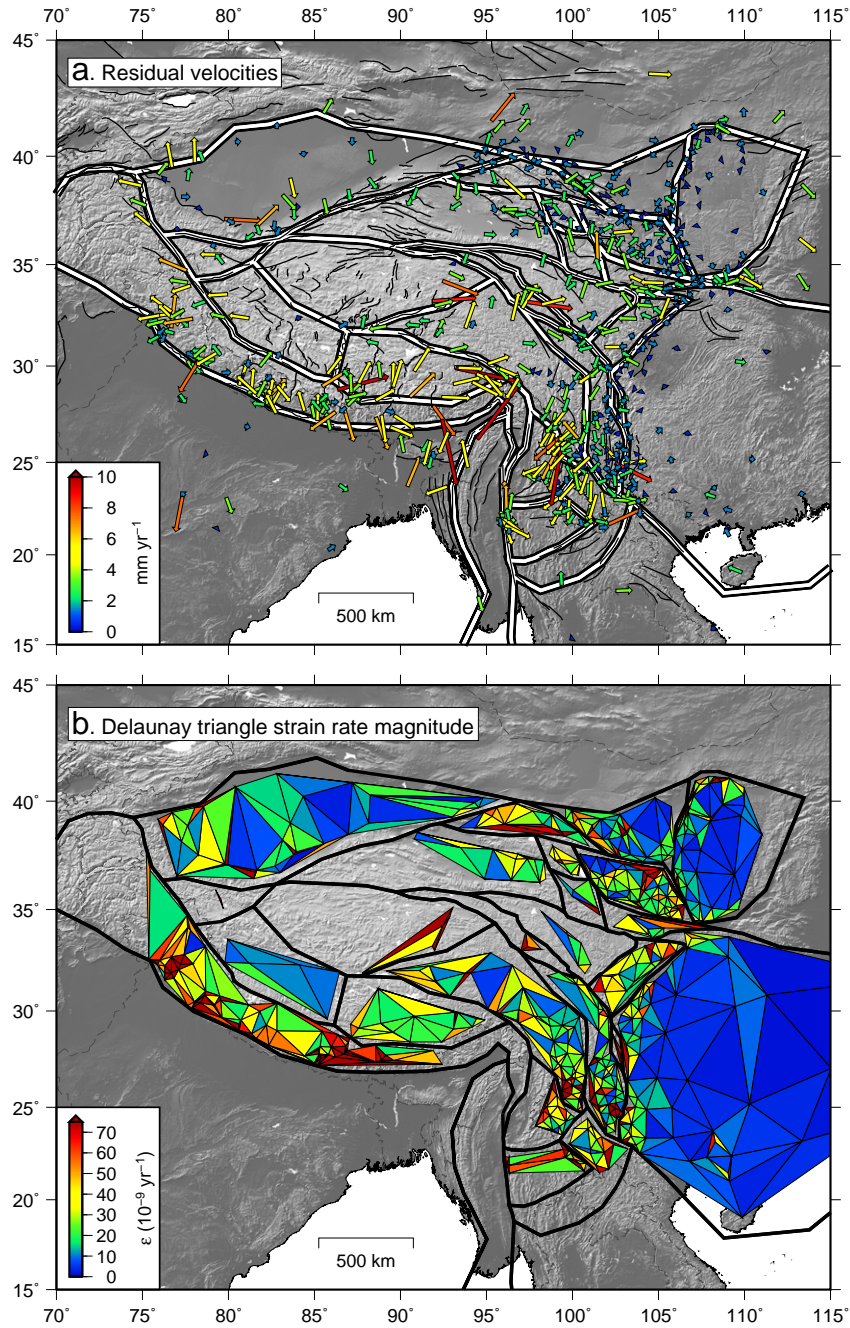


Fig. 4. a) Residual velocities from the joint geodetic–geologic inversion. Velocities are listed in Table S1. b) Delaunay triangulation of residual velocity field. Colors give the magnitude of the strain rate tensor within each triangle; we assume that strain is homogeneous within each element. Triangles whose sides cross block boundaries are discarded.

As an alternative to the residual velocity field gradient calculation of internal potency rate, we also estimate the best-fitting homogeneous spherical strain rate tensor, $\hat{\epsilon}_h$, for each micro-plate using an augmented Jacobian that explicitly includes a velocity field contribution from homogeneous strain (McCaffrey, 2005; Meade and Loveless, 2009; Savage et al., 2001) so that the intrablock potency rate, P_h , is

$$P_h = 2V_b |\hat{\epsilon}_h|. \quad (4)$$

The potency rate partitioning, ϕ , for the homogeneous internal micro-plate strain rate case is calculated with Eq. 1, replacing P_b with P_h .

The residual velocity field, $\hat{\mathbf{r}}$, used to calculate the internal block potency rates, P_b , includes contributions from unmodeled deforma-

tion and observational noise. To estimate the noise contribution to intrablock potency rates, we carry out Monte Carlo simulations using 1000 realizations of a synthetic observational noise velocity field, \mathbf{n} . In each trial, a synthetic velocity field is realized as the sum of the velocity field predicted by the joint inversion reference model, $\hat{\mathbf{v}}$, and noise, $\hat{\mathbf{v}}' = \hat{\mathbf{v}} + \mathbf{n}$. The predicted velocities $\hat{\mathbf{v}}$ are a function only of micro-plate rotations and earthquake cycle effects, with no contribution from observational noise (i.e., $P_b = 0$). For the north and east velocity components of each station, we generate Gaussian noise distributions with zero mean and standard deviation equal to the reported velocity component 1σ (67%) uncertainties, and one value is drawn from each of these distributions to generate \mathbf{n} . Therefore, in a given velocity field realization, \mathbf{n} itself is not necessarily a Gaussian distribution, as it reflects the different spreads of each velocity

component's distribution. We invert the noisy synthetic velocity field using the same block model and estimate the intrablock potency rate from the gradient of the resulting residual velocity field, $\hat{\mathbf{r}}'$. In this case, the residual velocity field is due entirely to observational noise, with no contribution from intrablock deformation. For each block, we calculate the proportion of trial internal block potency rates from the noise perturbation analysis, P_b^n , that are less than the rate from the standard residual velocity field analysis (Eq. 3) or homogeneous strain rate tensor estimation (Eq. 4) and term this quantity the internal deformation likelihood (IDL):

$$\text{IDL} = \frac{N(P_b^n < P_b)}{N_{\text{trials}}} \quad (5)$$

The IDL gives the likelihood that a fraction of P_b reflects deformation distinguishable from observational noise. We interpret blocks with high IDL as those that likely deform through physical mechanisms and processes not parametrized in the block model geometry. Conversely, the estimated internal potency rate of blocks with a zero or low IDL can be explained by the data noise contribution to the residual velocity field without unmodeled deformation sources.

The minimum magnitude of internal block deformation potency rate, $P_{ID} = P_b - \hat{P}_b^n$, that is likely to be distinguishable from that associated with observational noise can be determined by subtracting the median value from all Monte Carlo trials, \hat{P}_b^n , from the potency rate calculated from the joint inversion residual velocity field, P_b . We use these noise-corrected internal potency rates to determine the partitioning ratios, ϕ_{ID} (Eq. 1, substituting P_{ID} for P_b), that represent the amount of total deformation likely to be associated with intrablock deformation.

The joint geodetic–geologic inversion allows testing of spatial and temporal consistency between the different data types. First, we evaluate whether or not sparse geologic slip rates on faults across the Tibetan Plateau are consistent with micro-plate rotations. As possible explanations for the eastward decline in slip rate along the Kunlun fault, Kirby et al. (2007) suggested that slip may be transferred to adjacent structures and/or explained by differential rotation of crustal blocks north of the eastern Kunlun. The block model applies this concept to the entire plateau region, defining fault slip rates by projecting relative block rotations onto the three-dimensional fault system geometry. In a joint inversion, the rotations of adjacent blocks are coupled in two ways. Geologic observations define the slip rates on segments shared by two adjacent blocks, thereby constraining the relative rotational motion between them. Additionally, earthquake cycle effects across each fault segment contribute to GPS velocities, primarily at sites on the blocks sharing the boundary. The interseismic elastic deformation signal is a function of fault geometry and slip rate (e.g., Okada, 1985), and so velocities at GPS sites on adjacent blocks spanning a boundary fault place constraints on the slip rate and hence the rotational motion of the blocks. We also assess the temporal compatibility between the sparse geologic data, which describe fault slip averaged over thousands of years, and spatially denser GPS observations measuring surface deformation on decadal time scales. The fit to each constraining data set depends on the weighting applied in the least squares inversion: lower weighting of the geologic slip rates results in improved fits to GPS at the expense of poorer fits to the slip rates. A model that satisfies both data sets simultaneously indicates the spatial kinematic and temporal compatibility of geologic and geodetic observations.

3. Kinematically consistent fault slip rates in the Tibetan Plateau

A reference block model geometry (Fig. 1) based on fault network connectivity suggested by the Taylor and Yin (2009) active fault map defines 29 micro-plates of which 24 comprise the greater Tibetan Plateau region. The plateau blocks range in size from $1.1 \times 10^4 \text{ km}^2$ to

$3.4 \times 10^6 \text{ km}^2$, the smallest located between the Anninghe and Daliangshan segments of the Xianshuihe–Xiaojiang (XS in Fig. 1) fault system ($27^\circ\text{--}29^\circ\text{N}$) and the largest making up much of southeast China. (See description of block geometry in Appendix A.) All fault segments are assumed to dip vertically, except the Main Frontal Thrust (MFT) and Longmenshan fold-and-thrust belt (LM), which have dips of 7°N and 20°W , respectively. Observations used to constrain the reference block model are nominally interseismic GPS velocities at 731 stations derived from five networks (Fig. 2, Table S1; Apel et al., 2006; Banerjee et al., 2008; Calais et al., 2006; Gan et al., 2007; Vigny et al., 2003), combined by minimizing the residual velocities at collocated stations using a 6-parameter (rotation and translation) transformation. In addition, we use 9 geologically constrained Holocene–Late Quaternary slip rates with reported uncertainties on individual faults (Fig. 3, Table 1; Brown et al., 2002; Cowgill, 2007; Haibing et al., 2005; Kirby et al., 2007; Lavé and Avouac, 2000; Li et al., 2009; Van der Woerd et al., 2002; Wen et al., 2003). Aside from those used as constraints in our model, other estimates of long-term slip rates exist for several major faults in the region, most notably the Altyn Tagh (e.g., Mériaux et al., 2004, 2005; Washburn et al., 2001), Haiyuan (Lasserre et al., 1999, 2002), and Karakoram (e.g., Chevalier et al., 2005). The slip rates on these faults are debated, and some in fact have been used to support models of discrete, block-like or continuous deformation (e.g., Jade et al., 2004). Where multiple estimates are available, we select the slower geologic slip rate constraints. In principle, this minimizes P_f by reducing fault slip rates, although use of faster slip rates as constraints may also yield poorer fits to the GPS data, thereby increasing P_b . We weight the geologic slip rate constraints 150 times more than the geodetic data, which results in approximately equal influence on the solution from the 9 geological data and the 1462 GPS observations (east and north velocity components at 731 stations, with uncertainties ranging from 0.1 to 4.8 mm/yr), assuming unit uncertainties on the slip rate constraints. Divergence-minimizing constraints are applied to all vertical faults within the plateau region to damp tensile motion; these constraints are weighted roughly 100 times less than the geologic slip rate constraints.

We find an optimal uniform locking depth of 16 km for all faults except the MFT, based on analysis of locking depth versus velocity residual statistics (Fig. 5a), which is broadly consistent with coseismic slip models for the 2001 Kokoxili (Kunlun) earthquake (Lasserre et al., 2005). Along the MFT, locking depths of 9.7, 15.5, and 14 km for western, central and eastern segments, respectively, best fit the GPS observations, assuming a uniform dip along strike (Fig. 5b); remaining large magnitude local residuals suggest that the fault may be more heterogeneously locked than assumed here. The weighted least squares inversion yields a fit to the GPS data with a mean residual velocity magnitude of 2.60 mm/yr and χ^2 per degree-of-freedom of 2.97, with 61% of residual magnitudes less than their 1-sigma uncertainties. These results indicate that geologic slip rates and their reported uncertainties, which range from 0.4 to 2 mm/yr, are kinematically consistent with micro-plate rotations and interseismic GPS velocities (see discussion; Fig. 6).

Combining sparse geologic data with the denser GPS velocity fields, we estimate left-lateral slip of 7.6 ± 0.6 – 7.9 ± 0.5 mm/yr on the multiple segments representing the Karakax fault (KX), 11.0 ± 0.1 – 11.3 ± 0.1 mm/yr on the central Altyn Tagh (AT) system, and 5.1 ± 0.6 mm/yr on the northeasternmost AT segment bounding the Qilian Shan block (G, Fig. 3). The central AT is constrained by an 11.7 ± 1.6 mm/yr rate (Cowgill, 2007; Cowgill et al., 2009), which lies between the minimum and maximum latest Quaternary (ca. 6 ka) slip rate estimates of 9.4 ± 0.9 and 13.7 ± 1.3 mm/yr (Cowgill et al., 2009). These slip rate constraints are indistinguishable, within uncertainties, from geodetically constrained rates (9 ± 4 – 5 mm/yr; Bendick et al., 2000; Wallace et al., 2004) but substantially slower than the late Pleistocene–Holocene rate proposed by (Mériaux et al., 2004, 26.9 \pm

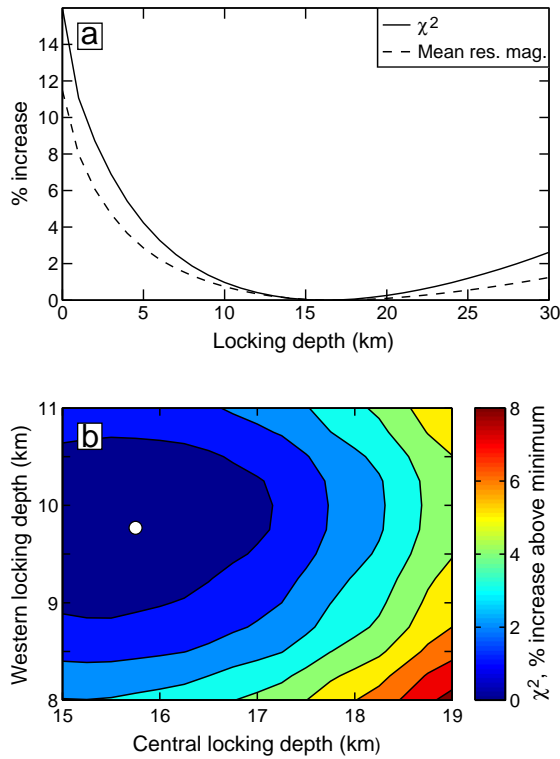


Fig. 5. Residual velocity statistics as a function of fault locking depth. a) We vary the locking depth of all plateau region faults, except those defining the Main Frontal Thrust (MFT), between 0 and 30 km and find that which minimizes the residual velocity field (16 km), here expressed as the percent increase above the minimum χ^2 value (solid) and mean residual velocity magnitude (dashed). b) Along the MFT, we find locking depths for the western, central, and eastern segments that best fit the GPS data, showing the χ^2 statistics for western and central segments holding the eastern segment at 14 km depth and all other plateau segments at the best-fitting 16 km depth.

6.9 mm/yr). Left-lateral slip rates are similarly constant along much of the Kunlun fault (KN), ranging from 9.3 ± 0.6 to 10.8 ± 0.0 mm/yr between the junctions with the AT and Elashan faults ($\sim 100^\circ\text{E}$ longitude) as constrained by two geologic rates (Haibing et al., 2005; Van der Woerd et al., 2002). Segmentation of the eastern KN by the intersections with the Elashan and Riyueshan faults permits the slow

slip constraints of Kirby et al. (2007) to be met (5.0 ± 0.4 and 2.0 ± 0.4 mm/yr): estimated left-lateral slip rates on the easternmost KN are $1.8 \pm 0.1 - 5.6 \pm 0.1$ mm/yr. In northeastern Tibet, we estimate $7.0 \pm 0.4 - 7.5 \pm 0.4$ mm/yr of left-lateral slip on the West Qinling fault, and on the Haiyuan fault (HY), we estimate left-lateral slip of $4.6 \pm 0.1 - 4.7 \pm 0.3$ mm/yr, constrained by the average Quaternary rate of 4.5 ± 1.1 mm/yr (Li et al., 2009). The faster estimated slip rates on the West Qinling and HY faults than on the eastern KN is consistent with the model of Duvall and Clark (2010) in which left-lateral slip is shifted north off of KN near its eastern extent. Our results suggest that the slip rate variations along strike KN can be explained by mechanical fault segmentation and differential micro-plate rotations, similar to the model proposed by Kirby et al. (2007). Along the Elashan fault, we estimate right-lateral slip of 1.0 ± 0.8 mm/yr (north) to 4.2 ± 0.4 mm/yr (south). On the subparallel Riyueshan fault, we estimate 0.9 ± 0.8 mm/yr left-lateral slip on the northern segment and 5.3 ± 0.5 mm/yr right-lateral slip on the segment south of the intersection with the West Qinling fault.

At the eastern margin of the Tibetan Plateau, the Xianshuihe–Xiaojiang fault system (XS) shows several branches and splays, including the Anninghe and Daliangshan segments, and Ganzi–Yushu fault (GY). Together, these faults accommodate a consistent rate of left-lateral slip from $23^\circ - 35^\circ\text{N}$. Slip on the segment south of the Anninghe–Daliangshan splay is $9.9 \pm 0.3 - 11.1 \pm 0.3$ mm/yr, slightly slower than the $13 - 15$ mm/yr rate across multiple branches of XS since the Late Pleistocene (Shen et al., 2003). To the north, slip is partitioned into $9.1 \pm 1.1 - 10.0 \pm 1.0$ mm/yr on the Anninghe segment and $1.7 \pm 1.1 - 2.3 \pm 1.1$ mm/yr on the Daliangshan segment. Northwest of these segments, XS slips at $9.6 \pm 0.5 - 11.6 \pm 0.3$ mm/yr. Slip is again partitioned northwest of the intersection between XS and GY, with central GY slipping $10.2 \pm 0.2 - 14.6 \pm 0.3$ mm/yr as constrained by the 12.0 ± 2.0 mm/yr constraint of Wen et al. (2003), and XS slipping more slowly, ranging from 0.6 ± 0.1 mm/yr right-lateral to 0.2 ± 0.2 mm/yr left-lateral, with several segment slip rates smaller than their estimated uncertainties. Northwest of the intersection with fault F3, GY slips left laterally up to 0.8 ± 0.5 mm/yr, with many segments showing statistically insignificant slip, slower than the ~ 7 mm/yr suggested by Wang et al. (2008), which we did not use as a constraint in the inversion owing to its lack of reported uncertainty. The along-strike change in and partitioning of the XS/GY slip rate as a consequence of fault segmentation and branching is similar to the

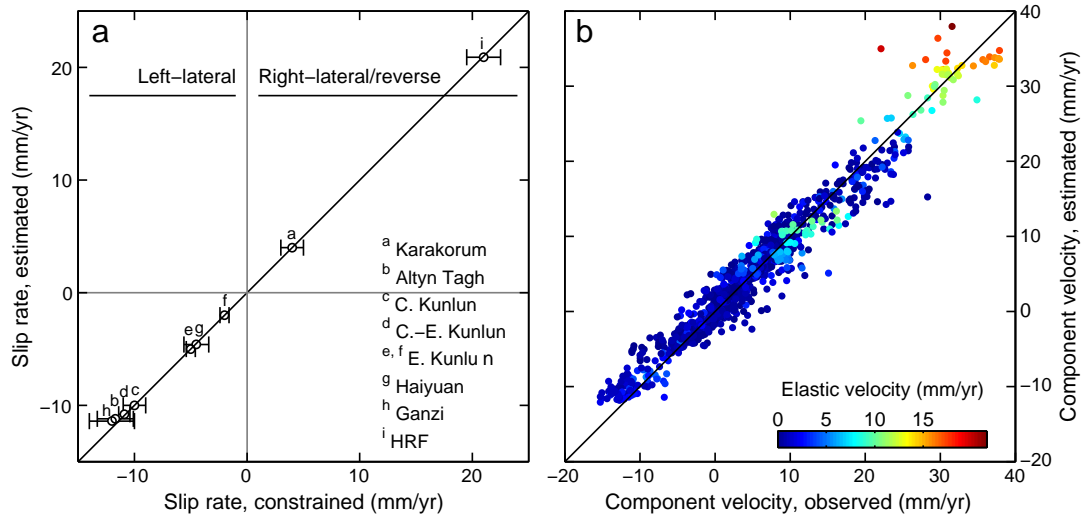


Fig. 6. Constraining and estimated geologic and geodetic data. a) Geologic fault slip rates used as constraints versus estimated rates. Reported uncertainties are shown; estimated uncertainties are not. Segments are labeled in Fig. 3. b) Observed versus estimated GPS component velocities within the plateau micro-plates. Color denotes magnitude of velocity contribution from elastic earthquake cycle processes. In both panels, a 1:1 relationship is given by the black line.

changes in slip rate on KN (Kirby et al., 2007) and the Big Bend region of the San Andreas fault in southern California (e.g., Meade and Hager, 2005).

Along the southeast margin of the plateau, estimated right-lateral motion on the Red River fault (RR) is up to 4.9 ± 0.4 mm/yr northwest of the intersection with XS, at the upper range of the 2–5 mm/yr Pliocene rate presented by Allen et al. (1984). Southeast of the XS intersection, RR slips right-laterally around 3.5 mm/yr. Estimated strike-slip on the Jiali fault (JI) is right-lateral, consistent with the sense of geologically recorded slip, but the estimated rates of 1.5 ± 0.4 – 2.5 ± 0.4 mm/yr are considerably slower than the 10–100 kyr 10–20 mm/yr right-lateral rates suggested by Armijo et al. (1989) across a suite of subparallel structures in this region on the basis of mapped offsets of inferred post-glacial landforms. However, we estimate faster right-lateral slip rates on F6, roughly coincident with the Indus Yalu suture zone (5.5 ± 0.4 – 9.8 ± 0.4 mm/yr), and on the continuation of JI around the eastern syntaxis (19.0 ± 0.3 – 20.1 ± 0.3 mm/yr). Right-lateral slip rates on the Karakorum fault (KM) are 3.0 ± 0.1 – 5.4 ± 0.3 mm/yr, while F1 slips right-laterally at 1.1 ± 0.6 – 3.4 ± 0.6 mm/yr. Taylor and Peltzer (2006) used satellite radar interferometry to estimate right-lateral slip of 2.1–4.1 mm/yr on the Lamu Co fault, located about 100 km southwest of F1. On KM between the Longmu–Gozha (LG) and KX intersections, we estimate statistically negligible right-lateral slip, but to the northwest, between the KX and Tien Shan (TS) intersections, we estimate left-lateral slip of 2.9 ± 0.4 – 5.5 ± 0.4 mm/yr. This is inconsistent with the geologically recorded sense of slip but is mechanically consistent with the clockwise rotation of the Tarim Basin, which rotates about an Euler pole located in the Qilian Shan (99.2°E , 38.2°N), predicting left-lateral slip on nearly all bounding faults. We estimate left-lateral slip of 13.3 ± 0.8 mm/yr on northeast LG (Gozha segment) and 2.7 ± 0.8 – 3.2 ± 0.8 on southwest LG (Longmu segment). The Gozha segment rate is similar to the Quaternary rate of 8.3 ± 2.7 mm/yr estimated by Raterman et al. (2007) based on a kinematic analysis of slip rates on AT, KX, and KM. We estimate left-lateral slip on F3 of 10.5 ± 0.5 – 12.4 ± 0.5 mm/yr.

Along the MFT, we estimate 10.7 ± 0.4 – 21.0 ± 0.2 mm/yr of reverse motion, from west to east, constrained by the 21.0 ± 1.5 mm/yr rate of Lavé and Avouac (2000) around 85°E longitude (Fig. 3b). The gradient in slip rates results from a local Euler pole of the Indo-Australian plate ($52.54 \pm 0.86^\circ\text{E}$, $36.60 \pm 0.93^\circ\text{N}$, $0.40 \pm 0.007^\circ/\text{Myr}$ relative to the Himalayan Range Front block, and $17.42 \pm 1.13^\circ\text{E}$, $27.09 \pm 0.32^\circ\text{N}$, $0.39 \pm 0.005^\circ/\text{Myr}$ relative to a nominally stable Eurasian GPS reference frame). The India–Eurasia pole is similar to previous geodetic estimates of $11.62 \pm 14.4^\circ\text{E}$, $28.56 \pm 1.1^\circ\text{N}$, $0.36 \pm 0.03^\circ/\text{Myr}$ (Sella et al., 2002), 17.65°W , 24.22°N , $0.32 \pm 0.02^\circ/\text{Myr}$ (Prawirodirdjo and Bock, 2004), and $13.99 \pm 7.8^\circ\text{E}$, $26.45 \pm 3.4^\circ\text{N}$, $0.35 \pm 0.02^\circ/\text{Myr}$ (Bettinelli et al., 2006). Across the Longmenshan fold-and-thrust belt, where there are no known geologic slip rate constraints, we estimate 3.2 ± 0.5 – 4.2 ± 0.4 mm/yr of reverse motion, along with 2.8 ± 0.3 – 3.5 ± 0.3 mm/yr of right-lateral slip, consistent with the oblique coseismic slip that characterized the 2007 Wenchuan earthquake both at depth (e.g., Feng et al., 2010) and at the surface (e.g., Xu et al., 2009).

4. Deformation partitioning in the Tibetan Plateau

The kinematically consistent slip rates reflect recent deformation of the Tibetan Plateau region occurring on the major structures included in the model under the assumption that decadal and

Quaternary rates are consistent through time. Block models are predicated on the idea that interseismic deformation as recorded at GPS stations is the result of micro-plate rotations and earthquake cycle processes along major faults. Residual GPS velocities, therefore, reflect unparametrized deformation. By comparing the potency rates on major faults (Eq. 2) to those calculated using the residual velocity field within each block (Eq. 3) through calculation of the potency rate partitioning value, ϕ (Eq. 1), the magnitude of deformation sources not associated with the block model geometry can be determined.

Potency rate partitioning values for the joint geodetic–geologic inversion, assuming no observational noise, range from $\phi = 0.27$ in the Himalayan Range block (labeled A in Fig. 1), where the fault area of the shallowly dipping MFT results in a large on-fault potency rate, to 0.91 in the Aksai Chin block (W; Fig. 7a). Aside from these blocks and the west-central plateau block (D, $\phi = 0.83$), ϕ is in the range of ~ 0.50 – 0.75 for all other tectonic micro-plates. Potency magnitude and partitioning values from an inversion of geodetic data alone, without the geologic fault slip rate constraints but considering divergence minimizing conditions, are similar to those from the joint geologic–geodetic inversion (Table 2; Fig. S1a), with a mean magnitude of change in partitioning ratio of 4.7% relative to the joint inversion values. Potency rate partitioning values calculated using the best-fitting homogeneous strain rate tensor estimate (e.g., McCaffrey, 2005) are an average of 45.7% lower than the values from the full residual velocity field gradient, averaging $\phi = 0.35$, and are lower in all blocks (Table 2; Fig. S2a).

The IDL (Eq. 5) can be interpreted as the likelihood that the internal block potency rate estimate reflects deformation distinguishable from the null hypothesis that residual velocities reflect only observational noise (Table 2; Fig. 7b). The frequency distributions of simulated noise potency rates from the Monte Carlo simulations are shown for select blocks in Fig. 7d–i. We estimate high IDL (~ 0.5 or greater) in the Himalayan Range (A), Jiali (C), west-central plateau (D), Ganzi–Xianshuihe sliver (N), Burma (U), and Aksai Chin (W) blocks and $\text{IDL} \leq 0.05$ in the east-central plateau (E), Qaidam Basin (F), most of the northeastern blocks (H, K, L, and M), the Lugu Lake (O), Eastern Kunlun (P), south China (S), and Tarim Basin (X) blocks. Intermediate values of IDL between ~ 0.1 and 0.4 characterize the Karakorum (B), Qilian Shan (G), Gonghe Nan Shan (I), West Qinling (J), Longmenshan (Q), Anninghe–Daliangshan (R), Yunnan (T), and Laos (V) blocks. The estimated IDL from the geodetic-only inversion differs from that of the joint inversion by <0.05 in general (Table 2). For the homogeneous estimated strain rate tensor calculation, we compare P_h with the P_h^0 values from the Monte Carlo simulation of data noise without estimating $\hat{\epsilon}_h$; IDL values are <0.1 for all blocks except the Jiali (C; 0.11) and Aksai Chin (W; 0.55) (Fig. S2b).

Zero to low IDL (<0.1) characterizes the Tarim Basin (block X), Qaidam Basin (block F), Ordos Plateau (block L), and south China (block S), including the Sichuan Basin. Internal potency rates in these and the other low IDL blocks cannot currently be distinguished from observational noise in the GPS data, without intrablock deformation. The lack of discernable internal deformation may be consistent with gravity-based studies suggesting greater elastic thickness beneath the Tarim and Qaidam Basins (Braitenberg et al., 2003) and regional tomographic studies indicating high seismic velocity roots beneath the Ordos Plateau and Sichuan Basin of the south China block (Yangtze Craton) (Lebedev and Nolet, 2003; Li et al., 2008).

High (greater than ~ 0.5) IDL blocks are likely to be accommodating deformation internally. The Himalayan Range Front block may not act as

Fig. 7. a) Potency rate partitioning values, ϕ , given as the intrablock percentage of the total potency rate, based on the gradient of the residual velocity field from the joint geodetic–geologic inversion. b) Internal deformation likelihood (IDL), given as the percent of Monte Carlo simulation trials whose intrablock potency rate magnitude is less than the rate from the reference model residual velocity gradient. c) Percentage of total potency rate accommodated by internal deformation that is statistically distinct from observational noise, ϕ_{ID} . d–i). Example histograms showing the frequency distribution of intrablock potency rates from the 1000 Monte Carlo trials. The corresponding blocks are labeled in panel b. In each of the histogram panels, the black solid curve shows the best-fitting Gaussian distribution of the histogram and the black dashed line shows the actual potency rate from the joint inversion. The mean (median) and standard deviation of the distribution, and the actual potency rate, are given as μ , σ , and A , respectively.

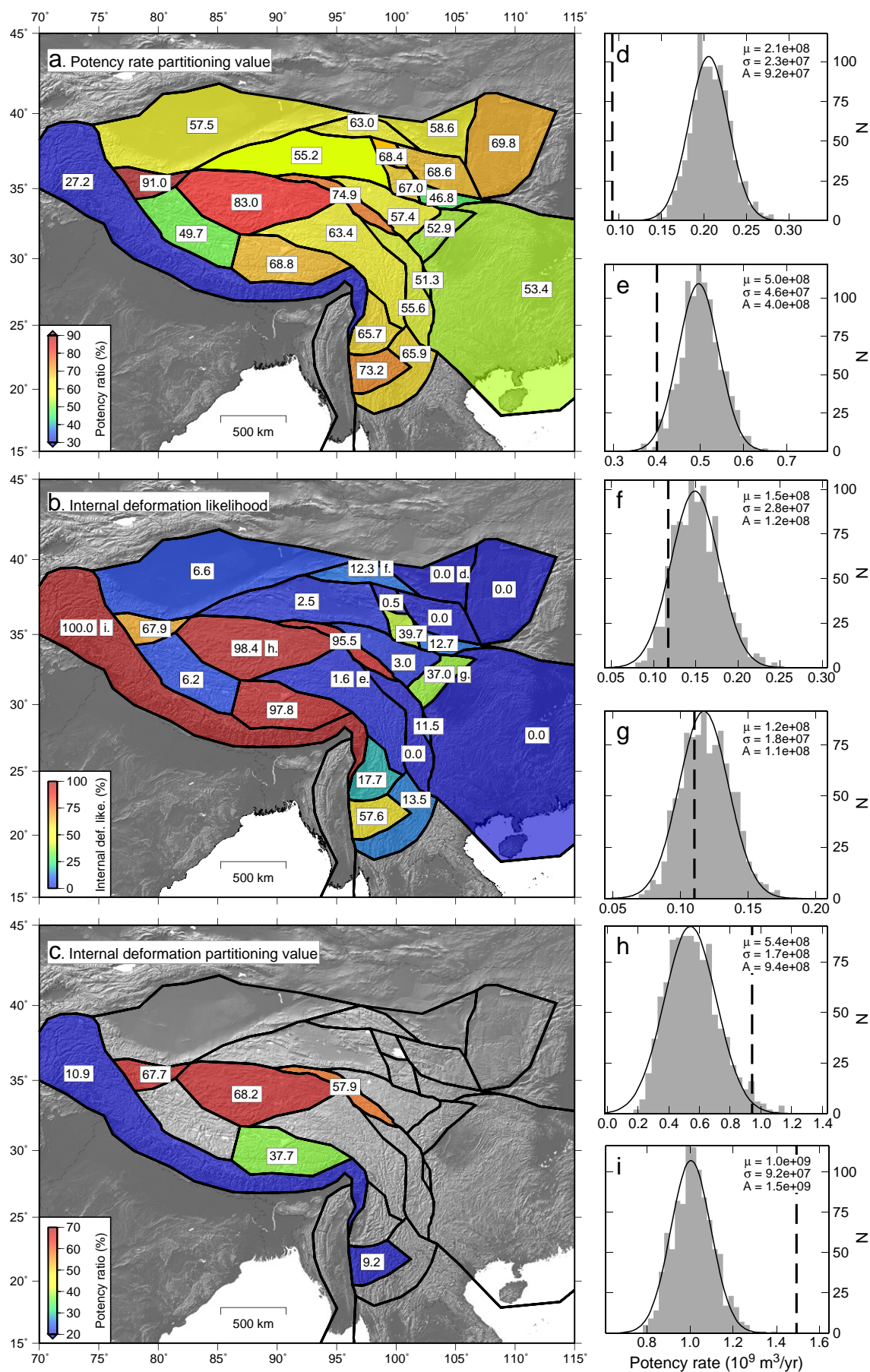


Table 2
Summary of potency rate partitioning parameters, expressed here as percentages.

Block ^a	Name	Joint inversion ^b			Geodetic-only ^c		Est. strain rate ^d	
		ϕ	IDL	ϕ_{ID}^b	ϕ	IDL	ϕ	IDL
A	Himalayan Range	27.2	100.0	10.9	27.5	100.0	2.9	0.0
B	Karakorum	49.7	6.2	0.0	48.9	6.2	48.9	1.6
C	Jiali	68.8	97.8	37.7	69.1	97.9	60.6	10.9
D	West-central Plateau	83.0	98.4	68.2	82.6	98.7	50.6	0.4
E	East-central Plateau	63.4	1.6	0.0	63.7	1.4	44.8	0.0
F	Qaidam Basin	55.2	2.5	0.0	58.5	1.9	31.4	0.0
G	Qilian Shan	63.0	12.3	0.0	66.4	12.5	16.2	0.0
H	Elashan	68.4	0.5	0.0	74.9	0.9	42.9	0.0
I	Gonghe Nan Shan	67.0	39.7	0.0	73.1	31.3	38.8	0.6
J	West Qinling	46.8	12.7	0.0	55.7	4.3	19.8	0.0
K	Haiyuan	58.6	0.0	0.0	58.8	0.0	13.0	0.0
L	Ordos Plateau	69.8	0.0	0.0	69.8	0.0	33.0	0.0
M	Lanzhou	68.6	0.0	0.0	72.0	0.0	26.8	0.0
N	Ganzi–Xianshuihe	74.9	95.5	57.9	67.5	89.5	44.0	5.8
O	Lugu Lake	55.6	0.0	0.0	59.6	0.0	19.7	0.0
P	Eastern Kunlun	57.4	3.0	0.0	51.0	2.4	45.1	0.1
Q	Longmenshan	52.9	37.0	0.0	56.6	33.6	11.3	0.0
R	Anninghe–Daliangshan	51.3	11.5	0.0	56.4	16.0	20.9	0.1
S	South China	53.4	0.0	0.0	54.7	0.0	10.4	0.0
T	Yunnan	65.7	17.7	0.0	66.0	15.5	54.4	0.0
U	Burma	73.2	57.6	9.2	73.1	57.6	52.1	0.0
V	Laos	65.9	13.5	0.0	66.4	12.9	62.3	1.1
W	Aksai Chin	91.0	67.9	67.7	92.2	67.8	88.4	55.1
X	Tarim Basin	57.5	6.6	0.0	60.0	5.0	11.7	0.0

Superscripts refer to information contained in corresponding figures: ^aFig. 1; ^bFig. 7; ^cFig. S1; ^dFig. S2; ^eFig. 7c.

a contiguous unit between the western to eastern syntaxes but may be segmented by normal faults striking roughly orthogonal to the HRF (e.g., Langin et al., 2003). Additionally, other thrust faults subparallel to the MFT may accommodate varying amounts of shortening along strike and, if considered in a model, could serve to reduce residual velocities. Our grid search suggests spatially variable locking depths along the MFT, but local residual velocities suggest that the pattern of elastic strain accumulation maybe more heterogeneous along strike, as suggested by (Bettinelli et al., 2006). Structures striking approximately north–south may also segment the Jiali block (C): residual velocity vectors suggest that a north striking normal fault around the longitude of Lhasa (90°E) may divide the block, such as the Yadong–Gulu rift considered by (Chen et al., 2004). Including such a structure reduces the magnitude and systematic orientation of residual velocities but predicts left-lateral slip on the Jiali fault, opposite the sense inferred from geologic observations (e.g., Armijo et al., 1989). Including the Riyueshan fault between the Gonghe Nan Shan and West Qinling blocks (I and J) reduces the magnitude of residual velocities relative to a test model in which the fault is absent while improving the agreement between estimated slip rates and geologic constraints (Kirby et al., 2007) on segments of the eastern KN. Deformation within these modeled micro-plates may alternatively be accommodated on multiple discrete structures, such as the thrust faults near 103°E, 35°N (Qinghai Bureau of Geology and Mineral Resources of Qinghai Province, 1991). The west-central plateau block (D) also shows large magnitude, systematically east trending residual velocities (Fig. 4a), which may suggest that additional structures divide the block into smaller parts that rotate independently. While there are several candidate structures for doing so (Fig. 1), GPS data in this region are sparsely distributed and so slip rates on such structures would be poorly resolved. In the Ganzi–Xianshuihe sliver block (N), large residual velocities (mean magnitude >5.2 mm/yr) and IDL ≥ 0.90 are found in both the joint geologic–geodetic and geodetic-only inversions, suggesting that some internal deformation takes place within this block and/or the reference block geometry is locally incorrect.

The internal deformation potency rate currently distinguishable from observational noise, P_{ID} , is positive for only the Himalayan

Range, west-central plateau, Jiali, Ganzi–Xianshuihe, Burma, and Aksai Chin blocks (2; Fig. 7c). Only these blocks must contribute to the diffuse deformation budget of the Tibetan Plateau. The total internal deformation potency rate partitioning ratio throughout the entire plateau region, $\phi_{plateau}$, given as

$$\phi_{plateau} = \frac{\sum P_{ID}}{\sum P_{ID} + \sum P_F}, \quad (6)$$

where P_{ID} is set to zero in those blocks with IDL ≤ 0.5 (i.e., where P_b exceeds P_b^0 in fewer than 50% of simulations) and the sums are taken over all plateau blocks, is 0.15, meaning that as much as 85% of observed deformation can be ascribed to the major faults included in the reference block model when observational noise is formally considered. A minimum bound on $\phi_{plateau}$ is given by assuming that data noise is negligible, and therefore P_{ID} is replaced with P_b in the numerator and denominator of Eq. (6). Using this modified expression gives $\phi_{plateau} = 0.51$, indicating that internal deformation would be required to explain about half of the geodetically observed deformation in the absence of data noise.

Estimates of intrablock and on-fault potency rates are a function of the realized fault system geometry. In the reference block model geometry, we included select structures whose continuity is currently unclear in order to reduce the systematic orientation and large magnitude of some clusters of residual velocity vectors. Excluding certain structures reduces the overall quality of fit to the GPS data, which in general yields larger P_b , ϕ , IDL, and ϕ_{ID} . Removing faults F1 and F3 results in a central Tibet block ~10⁶ km² in area. A test joint inversion using this fault system geometry estimates slip rates similar to the reference model, but with a faster western KN (~14.5 mm/yr left-lateral), faster KM (up to ~8 mm/yr right-lateral), left-lateral JI (up to 3.3 mm/yr right-lateral), and LG and northwestern GY that are consistent in slip rate along strike (~13–14 mm/yr and ~5 mm/yr left-lateral, respectively). The test model gives $\phi = 0.72$ for the central block (Fig. S3), slightly greater than the volume-weighted average of the partitioning values in the three corresponding blocks of the reference geometry ($\phi = 0.68$). The IDL of the combined central plateau block is 0.89, suggesting the importance of the additional active structures included in the reference model. IDL in the Karakorum (B) and east-central plateau (E) blocks of the reference model is notably lower (0.06 and 0.02, respectively) than that in the west-central plateau block (D, 0.98), which suggests that further subdivision of the west-central plateau block may be possible with the advent of sufficient geodetic and/or geologic data. The comparison between the degraded and reference models serves as an example of how the potency rate partitioning analysis can guide the identification of potentially active fault system structures.

Despite moderate to high IDL in the Anninghe–Daliangshan sliver (0.12), Aksai Chin block (0.68), and Ganzi–Xianshuihe sliver (0.96), internal potency rates may not represent internal deformation and may instead be an artifact of the strain calculation: at most three Delaunay strain rate triangles can be constructed from the GPS stations that lie within these blocks. The standard deviations of the Monte Carlo simulated potency rates in these blocks are the greatest of all blocks, exceeding 40% of the mean trial potency rate, P_b (as compared to a mean of 18.3% for all other blocks and 21.9% for all blocks). Trial intrablock potency rate variance decreases with the number of stations in the blocks (Fig. S4a) and in general decreases with increasing proportion of block volume represented by Delaunay triangles (Fig. S4b).

5. Potency rates and earthquake moment release

As an independent indicator of the partitioning between localized and diffuse deformation, we examine the spatial distribution of earthquakes in the Global CMT catalog since 1976 and a 20th century

historical catalog (Holt et al., 1995), calculating the distance between each event and the closest block boundary in the reference model (Fig. 8). In the CMT catalog, 476 earthquakes with depth ≤ 33 km and $M_W \geq 5.0$ have occurred within the plateau blocks, half of which were within 50 km of a modeled boundary (Fig. 9a). Sixty-seven percent of the cumulative moment release since 1976 has occurred in events within 25 km of a block boundary, and 90% within 93.1 km (Fig. 9b). Thirty-six major ($M_W \geq 6.4$) historical earthquakes have occurred since 1900 (Chen and Molnar, 1977; Holt et al., 1995) in the plateau blocks, 25 of which have been located within 50 km of the nearest block boundary (Fig. 9c). Assuming that the two $M_W = 8.3$ Himalayan Range Front events of 1905 and 1934, and the 1950 $M_W = 8.5$ Medog earthquake took place on the MFT (e.g., Bilham et al., 2001), which dips beneath the events' epicenters (i.e., segment-earthquake distance of zero), 90% of the cumulative historic moment release was released within 25.1 km of faults in the reference block model (Fig. 9d). The mean block length scale is defined as half the square root of the mean block area, reflecting the average distance from a block center to its boundaries, and for the reference model is 215 km (red vertical line in Fig. 9), roughly 9 times larger than the 25 km within which 82% of combined historical and modern moment has been released. We suggest that earthquakes located within ~ 25 km of a block boundary can be considered to have occurred on a modeled fault segment, given errors in earthquake location and the approximations we make in generating the block geometry from the discontinuous active fault map. Earthquake locations deduced from satellite interferometry suggest that, in remote locations, uncertainties in CMT locations may be as much as ~ 40 – 50 km (Lohman and Simons, 2005; Pritchard et al., 2006).

To examine the statistical significance of the distance–moment relationship, we randomly distribute the 476 modern and 36 historical earthquakes within the plateau blocks (excluding the South China block), retaining each event magnitude but assigning the epicenter a random location, and calculate the distance from any fault at which cumulative moment release reached 90%. Given 1000 trials of randomly seeded earthquake locations, we find that the 90% CMT moment distance in 71.4% of trials exceeds the actual distance, while the actual 90% historical moment distance is exceeded in 99.8% of trials. By carrying out this analysis, we test the hypothesis that

earthquake and hence crustal deformation is diffusely distributed throughout the Tibetan Plateau region and find that the true distribution of earthquakes is statistically likely to reflect deformation localized on the major faults included in the reference block model.

That 67% of all modern and $\sim 90\%$ of historical moment release occurred within 25 km of modeled fault segments (Fig. 9) indicates that the block boundaries chosen for our reference model represent the most important structures in the Tibetan Plateau region in terms of seismic moment release. This proximity of seismic moment release to major faults in Tibet, independent of geodetic data and the mechanical assumptions of the block model, provides an additional evidence for the importance of major faults in accommodating active deformation. The moment released more than 25 km from block model boundaries can be interpreted as intrablock deformation occurring on faults below the resolution of the model and could be used to guide changes to the model geometry, particularly in places where active fault maps based on field geology may be incomplete.

6. Discussion

We have shown that both Holocene–Quaternary geologic slip rates and decadal interseismic GPS velocities are consistent with a model of Tibet composed of rotating tectonic micro-plates. Estimates of fault slip and internal block strain rates provide the constraints necessary to quantitatively determine the potency rates associated with localized and diffuse crustal deformation. Given current geodetic coverage and sparse geologic slip rate estimates, internal block deformation is statistically distinguishable from observational noise only within the Himalayan Range, Jiali, west-central plateau, Ganzi–Xianshuihe sliver, Burma, and Aksai Chin blocks. These models suggest that fault slip on the boundaries of 24 micro-plates, interseismic elastic strain accumulation, and consideration of observational noise can describe 85% of surface motion of the greater Tibetan Plateau region as recorded in existing GPS data. Similarly, 82% of seismic moment release in the combined modern and historical earthquake catalog has occurred within 25 km of block model boundaries, offering additional evidence that major faults accommodate the majority of active deformation in Tibet.

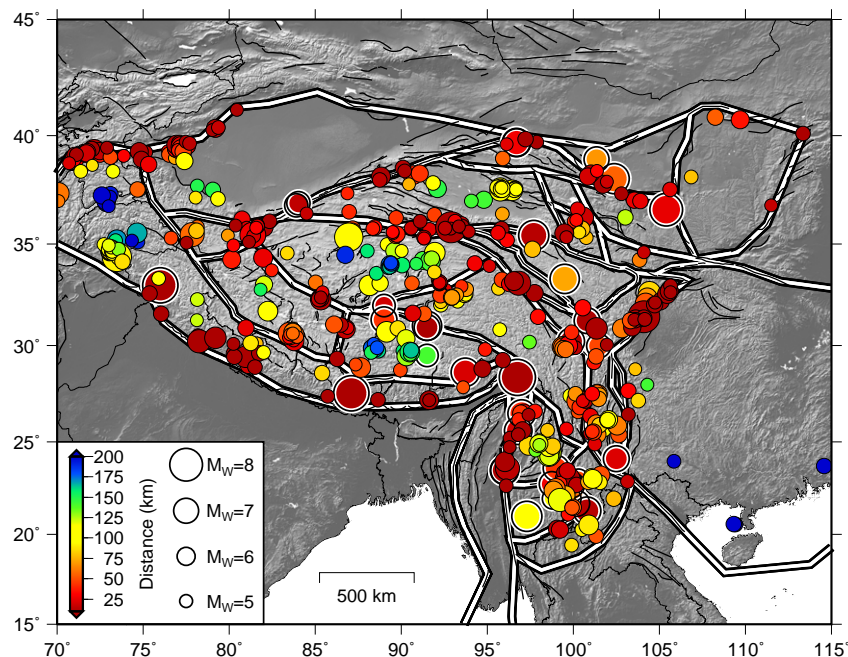


Fig. 8. Distance between modern (Global CMT catalog earthquakes with depth ≤ 33 km and $M_W \geq 5.0$) and historical (white outlined circles, $M_W \geq 6.4$ from Holt et al. (1995)) earthquakes and the surface trace of the nearest block geometry fault segment, scaled by magnitude. Only earthquakes within the greater plateau region are plotted.

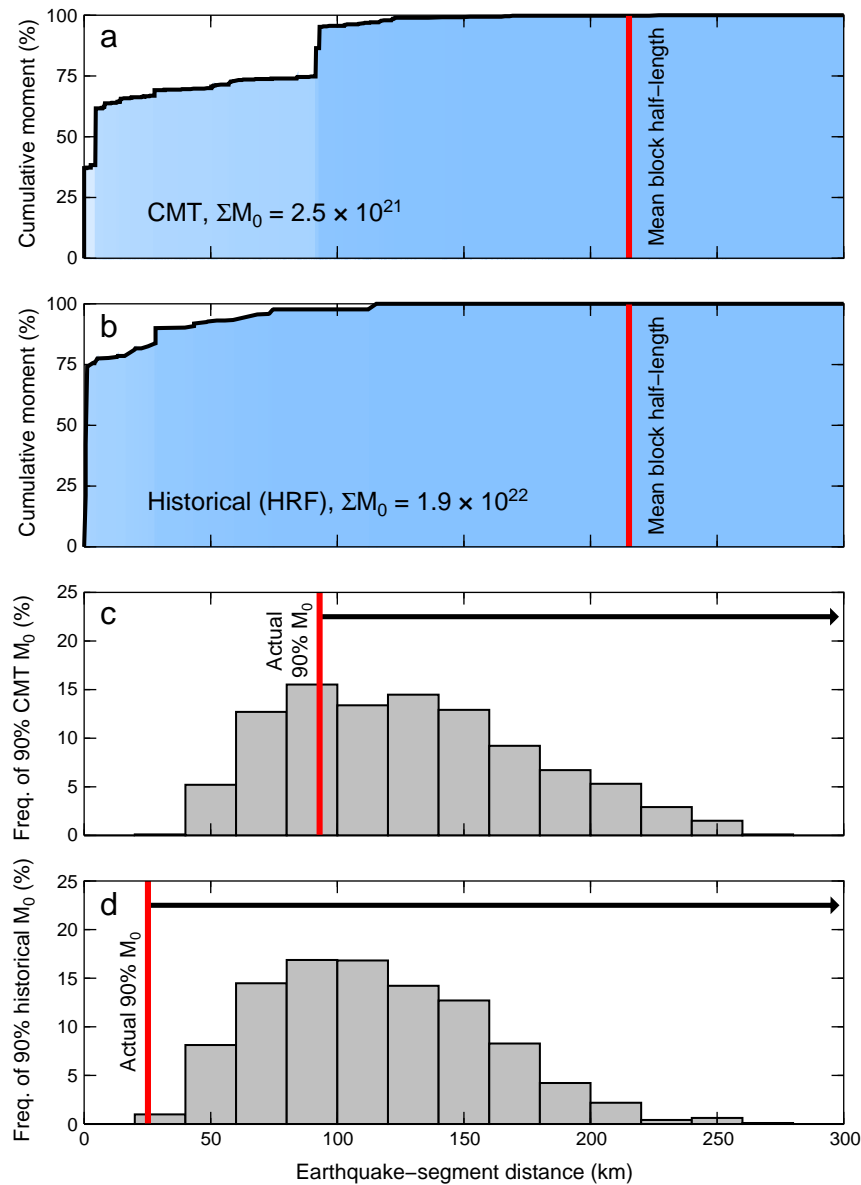


Fig. 9. Spatial distribution statistics of crustal earthquakes shown in Fig. 8. a, b) Cumulative moment of events within a given distance range of the nearest block geometry fault segment for modern (a) and historical (b) earthquakes. Ninety percent of the cumulative CMT moment occurred within 93.1 km of any block boundary and, assuming that the three largest historical earthquakes occurred on the dipping Himalayan Range Front (HRF) thrust, 90% of the historical moment was released within 25.1 km of block boundaries. The red vertical line represents a mean linear block dimension, given as half the mean of the square roots of the plateau blocks' areas (215 km), and represents an average distance between a block interior and its boundaries. c, d) To test the robustness of the moment–distance correlation, and to test the hypothesis that earthquakes represent diffuse deformation throughout the region, we randomly seeded earthquake locations, assigned each event a moment from the actual CMT and historical catalogs, and calculated the distance from any block boundary at which 90% cumulative moment is released. In 71.4% of CMT moment trials and 99.8% of historical moment trials, the 90% moment distance is reached at a distance greater than the corresponding distance from the actual catalog.

While block models provide a quasi-static earthquake cycle-based interpretation of recent plate boundary activity, fault system geometry evolves in response to finite displacements and so may not be considered stable over long periods of time (Cowgill et al., 2009; Taylor and Yin, 2009): some faults may become inactive, shifting activity onto adjacent structures, and fault intersections change as the micro-plates they bound undergo finite rotations. Here we have made the assumption that time variation in fault slip rates, from decadal to Quaternary scales, is negligible. While time variable fault activity has been documented in western North America (Dolan et al., 2007; Friedrich et al., 2003), geologic evidence for such behavior in Tibet (for example, along the Karakorum fault) is equivocal due to conflicting slip rate estimates over similar time periods (Brown et al., 2002; Chevalier et al., 2005). The result that both decadal geodetic velocities sampled only

over a fraction of an individual earthquake cycle and Holocene–Quaternary fault slip rates integrated over multiple earthquake cycles can be simultaneously satisfied using a micro-plate rotation model suggests that this assumption cannot be proven false at the scale of this study. The addition of spatially denser GPS observations and further field study of active faults may allow for the resolution of structures that accommodate the 15% of deformation not accounted for by the major structures in the reference model. Presently, it is unclear in which direction the potency partitioning would shift: newly collected geodetic and geologic data may resolve deformation on specific faults or may be consistent with diffuse deformation below the limit of detection. The inference that the majority of active deformation is localized along major faults provides a view of continental deformation as complex but increasingly resolvable.

Supplementary materials related to this article can be found online at doi:10.1016/j.epsl.2010.12.014.

Appendix A. Reference model block geometry description

The Himalayan Range block (block A in Fig. 1) is bounded by the Main Frontal Thrust (MFT) and the Karakorum fault (KM); we model KM as extending east of 85°E, roughly parallel to the MFT. Both faults bend around the eastern syntaxis at Namche Barwa, merging with the Sagaing fault (SG) and Burman Range Front (BRF) around 95°E. Immediately north of the Himalayan Range block, we model the Karakorum (B) and Jiali (C) blocks, bounded to the south by KM and its eastern extension and to the north by the Jiali fault (JI) and its westward continuation (F1) beyond 85°E, which follows a few short mapped fault segments. Separating the Karakorum and Jiali blocks at 85°E is a north–south striking structure (F2) mapped by Taylor and Yin (2009) as a series of normal faults. North of these blocks are the west-central plateau and east-central plateau blocks (D and E, respectively), bounded to the north by the western Kunlun fault (KN) and the Ganzi–Yushu fault (GY). Separating blocks the west- and east-central plateau blocks is a northeast striking structure (F3) connecting JI to GY, which follows a discontinuous trace on the active fault and modern seismicity maps (Taylor and Yin, 2009). North of the west-central plateau blocks, bounded by the Kunlun fault on the south, the Altyn Tagh fault (AT) on the west, and faults of the Qaidam thrust belt to the north, is the Qaidam Basin block (F). To its north is the Qilian Shan block (G), and to the east are the Elashan (H), Gonghe Nan Shan (I), West Qinling (J), Haiyuan (K), Ordos Plateau (L), and Lanzhou (M) blocks, whose boundaries are defined by reasonably contiguous fault networks, including the Haiyuan fault (HY). To the north and east of the east-central plateau block are the Ganzi–Xianshuihe sliver (block N) and Lugu Lake block (O), whose boundaries are KN, GY and a south–southeast striking branch (F4) leading to the Red River fault (RR), and the Xianshuihe fault (XS). The Eastern Kunlun block (P) is triangular in shape and lies between the eastern KN, northern XS, and the fault (F5) west of the Longmenshan fold-and-thrust belt (LM); east of the Eastern Kunlun block is the Longmenshan proper (block Q). The Anninghe–Daliangshan block (R) lies between two segments of the XS, and the south China block (S) lies to its east. The Yunnan (T), Burma (U), and Laos (V) blocks are located in southeast Asia, where GPS data are sparse. The Aksai Chin block (W) is located about 80°E, between the Longmu–Gozha fault (LG), the Karakax fault (KX), and the western KM. Finally, the Tarim Basin block (X) lies between KX, AT, and the southern edge of the Tien Shan (TS).

Acknowledgments

We thank Jean-Philippe Avouac, an anonymous referee, and editor Rob van der Hilst for helpful comments. This work was supported by funding from Harvard University.

References

- Aki, K., Richards, P.G., 1980. Quantitative Seismology: Theory and Methods, vol. 1. W. H. Freeman, San Francisco. 557 pp.
- Allen, C.R., Gillespie, A.R., Yuan, H., Sieh, K.E., Buchan, Z., Chengnan, Z., 1984. Red River and associated faults, Yunnan Province, China: Quaternary geology, slip rates, and seismic hazard. *Geol. Soc. Am. Bull.* 95 (6), 686–700. doi:10.1130/0016-7606(1984)95<686:RRAAFY>2.0.CO;2.
- Apel, E.V., Burgmann, R., Steblov, G., Vasilenko, N., King, R., Prytkov, A., 2006. Independent active microplate tectonics of northeast Asia from GPS velocities and block modeling. *Geophys. Res. Lett.* 33, L11303. doi:10.1029/2006GL026077.
- Armijo, R., Tapponnier, P., Tonglin, H., 1989. Late Cenozoic right-lateral strike-slip faulting in southern Tibet. *J. Geophys. Res.* 94 (B3), 2787–2838.
- Avouac, J.P., Tapponnier, P., 1993. Kinematic Model of Active Deformation in Central-Asia. *Geophys. Res. Lett.* 20 (10), 895–898.
- Banerjee, P., Bürgmann, R., Nagarajan, B., Apel, E., 2008. Intraplate deformation of the Indian subcontinent. *Geophys. Res. Lett.* 35, L18301. doi:10.1029/2008GL035468.
- Bendick, R., Bilham, R., Freymueller, J., Larson, K., Yin, G.H., 2000. Geodetic evidence for a low slip rate in the Altyn Tagh fault system. *Nature* 404 (6773), 69–72.
- Bennett, R.A., Rodi, W., Reilinger, R.E., 1996. Global positioning system constraints on fault slip rates in southern California and northern Baja, Mexico. *J. Geophys. Res.* 101 (B10), 21943–21960.
- Bettinelli, P., Avouac, J.-P., Flouzat, M., Jouanne, F., Bollinger, L., Willis, P., Chitrakar, G.R., 2006. Plate motion of India and interseismic strain in the Nepal Himalaya from GPS and DORIS measurements. *J. Geodesy* 80, 567–589. doi:10.1007/s00190-006-0030-3.
- Bilham, R., Larson, K., Freymueller, J., Jouanne, F., LeFort, P., Leturmy, P., Mugnier, J.L., Gamond, J.F., Glot, J.P., Martinod, J., Chaudury, N.L., Chitrakar, G.R., Gautam, U.P., Koirala, B.P., Pandey, M.R., Ranabhat, R., Sapkota, S.N., Shrestha, P.L., Thakuri, M.C., Timilsina, U.R., Tiwari, D.R., Vidal, G., Vigny, C., Galy, A., deVoogd, B., 1997. GPS measurements of present-day convergence across the Nepal Himalaya. *Nature* 386 (6620), 61–64.
- Bilham, R., Gaur, V.K., Molnar, P., 2001. Himalayan Seismic Hazard. *Science* 293 (5534), 1442–1444.
- Braitenberg, C., Wang, Y., Fang, J., Hsu, H., 2003. Spatial variations of flexure parameters over the Tibet–Qinghai plateau. *Earth Planet. Sci. Lett.* 205 (3–4), 211–224. doi:10.1016/S0012-821X(02)01042-7.
- Brown, E.T., Bendick, R., Bourles, D.L., Gaur, V., Molnar, P., Raisbeck, G.M., Yiou, F., 2002. Slip rates of the Karakorum fault, Ladakh, India, determined using cosmic ray exposure dating of debris flows and moraines. *J. Geophys. Res.* 107 (B9), 2192. doi:10.1029/2000JB000100.
- Calais, E., Dong, L., Wang, M., Shen, Z., Vergnolle, M., 2006. Continental deformation in Asia from a combined GPS solution. *Geophys. Res. Lett.* 33, L24319. doi:10.1029/2006GL028433.
- Chen, W.-P., Molnar, P., 1977. Seismic moments of major earthquakes and average rate of slip in central Asia. *J. Geophys. Res.* 82 (20), 2945–2969.
- Chen, Q.Z., Freymueller, J.T., Wang, Q., Yang, Z.Q., Xu, C.J., Liu, J.N., 2004. A deforming block model for the present-day tectonics of Tibet. *J. Geophys. Res.* 109 (B1), B01403. doi:10.1029/2002JB002151.
- Chevalier, M.L., Ryerson, F.J., Tapponnier, P., Finkel, R.C., Van der Woerd, J., Li, H.B., Liu, Q., 2005. Slip-rate measurements on the Karakorum Fault may imply secular variations in fault motion. *Science* 307 (5708), 411–414.
- Cowgill, E., 2007. Impact of riser reconstructions on estimation of secular variation in rates of strike-slip faulting: Revisiting the Chertchen River site along the Altyn Tagh Fault, NW China. *Earth Planet. Sci. Lett.* 254, 239–255. doi:10.1016/j.epsl.2006.09.015.
- Cowgill, E., Gold, R.D., Xuanhua, C., Xiao-Feng, W., Arrowsmith, J.R., Southon, J., 2009. Low Quaternary slip rate reconciles geodetic and geologic rates along the Altyn Tagh fault, northwestern Tibet. *Geology* 37 (7), 647–650. doi:10.1130/G25623A.1.
- Dolan, J., Bowman, D., Sammis, C., 2007. Long-range and long-term fault interactions in Southern California. *Geology* 35 (9), 855–858. doi:10.1130/G23789A.1.
- Duvall, A.R., Clark, M.K., 2010. Dissipation of fast strike-slip faulting within and beyond northeastern Tibet. *Geology* 38 (3), 223–226. doi:10.1130/G30711.1.
- England, P., Molnar, P., 2005. Late Quaternary to decadal velocity fields in Asia. *J. Geophys. Res.* 110 (B12), B12401. doi:10.1029/2004JB003541.
- Feldt, N., Bilham, R., 2006. Great Himalayan earthquakes and the Tibetan plateau. *Nature* 444, 165–170. doi:10.1038/nature05199.
- Feng, G., Hetland, E.A., Ding, X., Li, Z., Zhang, L., 2010. Coseismic fault slip of the 2008 mw 7.9 wenchuan earthquake estimated from insar and gps measurements. *Geophys. Res. Lett.* 37 (1), L01302. doi:10.1029/2009GL041213.
- Flesch, L.M., Haines, A.J., Holt, W.E., 2001. Dynamics of the India-Eurasia collision zone. *J. Geophys. Res.* 106 (B8), 16435–16460.
- Friedrich, A.M., Wernicke, B.P., Niemi, N.A., Bennett, R.A., Davis, J.L., 2003. Comparison of geodetic and geologic data from the Wasatch region, Utah, and implications for the spectral character of Earth deformation at periods of 10 to 10 million years. *J. Geophys. Res.* 108 (B4), 2199. doi:10.1029/2001JB000682.
- Gan, W., Zhang, P., Shen, Z.-K., Niu, Z., Wang, M., Wan, Y., Zhou, D., Cheng, J., 2007. Present-day crustal motion within the Tibetan Plateau inferred from GPS measurements. *J. Geophys. Res.* 112. doi:10.1029/2005JB004120.
- Haibing, L., Van der Woerd, J., Tapponnier, P., Klinger, Y., Xuexiang, Q., Jingsui, Y., Yintang, Z., 2005. Slip rate on the Kunlun fault at Hongshui Gou, and recurrence time of great events comparable to the 14/11/2001, Mw 7.9 Kokoxili earthquake. *Earth Planet. Sci. Lett.* 237 (1–2), 285–299. doi:10.1016/j.epsl.2005.05.041.
- Hilley, G.E., Burgmann, R., Zhang, P.Z., Molnar, P., 2005. Bayesian inference of plastosphere viscosities near the Kunlun Fault, northern Tibet. *Geophys. Res. Lett.* 32 (1), L01302. doi:10.1029/2004GL021658.
- Hilley, G.E., Johnson, K., Wang, M., Shen, Z.-K., Bürgmann, R., 2009. Earthquake-cycle deformation and fault slip rates in northern Tibet. *Geology* 37 (1), 31–34. doi:10.1130/G25157A.1.
- Holt, W.E., Li, M., Haines, A.J., 1995. Earthquake strain rates and instantaneous relative motions within central and eastern Asia. *Geophys. J. Int.* 122 (2), 569–593.
- Jade, S., Bhatt, B.C., Yang, Z., Bendick, R., Gaur, V.K., Molnar, P., Anand, M.B., Kumar, D., 2004. GPS measurements from the Ladakh Himalaya, India: Preliminary tests of plate-like or continuous deformation in Tibet. *Geol. Soc. Am. Bull.* 116 (11–12), 1385–1391.
- Kirby, E., Harkins, N., Wang, E., Shi, X., Fan, C., Burbank, D., 2007. Slip rate gradients along the eastern Kunlun fault. *Tectonics* 26, TC2010. doi:10.1029/2006TC002033.
- Kostrov, B.V., Das, S., 1988. Principles of earthquake source mechanics. Cambridge University Press, Cambridge. 286 pp.
- Langin, W.R., Brown, L.D., Sandvol, E.A., 2003. Seismicity of central 32 Tibet from Project INDEPTH III seismic recordings. *Bull. Seismol. Soc. Am.* 93 (5), 2146–2159. doi:10.1785/0120030004.
- Lasserre, C., Morel, P.-H., Gaudemer, Y., Tapponnier, P., Ryerson, F., King, G.C., Métivier, F., Kasser, M., Kashgarian, M., Baichi, L., Taiya, L., Daoyang, Y., 1999. Postglacial left

- slip rate and past occurrence of $M \geq 8$ earthquakes on the western Haiyuan fault, Gansu, China. *J. Geophys. Res.* 104 (B8), 17633–17651. doi:10.1029/1998JB900082.
- Lasserre, C., Gaudemer, Y., Tapponnier, P., Mériaux, A.-S., der Woerd, J.V., Daoyang, Y., Ryerson, F.J., Finkel, R.C., Caffee, M.W., 2002. Fast late Pleistocene slip rate on the Leng Long Ling segment of the Haiyuan fault, Qinghai, China. *J. Geophys. Res.* 107 (B11), 2276. doi:10.1029/2000JB000060.
- Lasserre, C., Peltzer, G., Crampé, F., Klinger, Y., Van der Woerd, J., Tapponnier, P., 2005. Coseismic deformation of the 2001 $M_w = 7.8$ Kokoxili earthquake in Tibet, measured by synthetic aperture radar interferometry. *J. Geophys. Res.* 110 (B12), B12408. doi:10.1029/2004JB003500.
- Lavé, J., Avouac, J.P., 2000. Active folding of fluvial terraces across the Siwaliks Hills, Himalayas of central Nepal. *J. Geophys. Res.* 105 (B3), 5735–5770.
- Lebedev, S., Nolet, G., 2003. Upper mantle beneath Southeast Asia from S velocity tomography. *J. Geophys. Res.* 108 (B1), 2048. doi:10.1029/2000JB000073.
- Li, C., van der Hilst, R.D., Meltzer, A.S., Engdahl, E.R., 2008. Subduction of the Indian lithosphere beneath the Tibetan Plateau and Burma. *Earth Planet. Sci. Lett.* 274, 157–168. doi:10.1016/j.epsl.2008.07.016.
- Li, C., Zhang, P., Yin, J., Min, W., 2009. Late Quaternary left-lateral slip rate of the Haiyuan fault, northeastern margin of the Tibetan Plateau. *Tectonics* 28, TC5010. doi:10.1029/2008TC002302.
- Lohman, R.B., Simons, M., 2005. Locations of selected small earthquakes in the Zagros mountains. *Geochim. Geophys. Geosyst.* 6 (1), Q03001. doi:10.1029/2004GC000849.
- Matsu'ura, M., Jackson, D.D., Cheng, A., 1986. Dislocation model for aseismic crustal deformation at Hollister, California. *J. Geophys. Res.* 91 (B12), 2661–2674.
- McCaffrey, R., 2002. Crustal block rotations and plate coupling. In: Stein, S., Freymueller, J.T. (Eds.), *Plate Boundary Zones*. : Geodynamics Series, vol. 30. American Geophysical Union, pp. 101–122. doi:10.1029/030GD06.
- McCaffrey, R., 2005. Block kinematics of the Pacific-North America plate boundary in the southwestern United States from inversion of GPS, seismological, and geologic data. *Journal of Geophysical Research*, 110, B7, p. B07401. doi:10.1029/2004JB003307.
- Meade, B.J., 2007. Present-day kinematics at the India-Asia collision zone. *Geology* 35 (1), 81–84. doi:10.1130/G22924A.1.
- Meade, B.J., Hager, B.H., 2005. Block models of crustal motion in southern California constrained by GPS measurements. *J. Geophys. Res.* 110, B03403. doi:10.1029/2004JB003209.
- Meade, B.J., Loveless, J.P., 2009. Block modeling with connected fault network geometries and a linear elastic coupling estimator in spherical coordinates. *Bull. Seismol. Soc. Am.* 99 (6), 3124–3139. doi:10.1785/0120090088.
- Mériaux, A.S., Ryerson, F.J., Tapponnier, P., Van der Woerd, J., Finkel, R.C., Xu, X., Xu, Z., Caffee, M.W., 2004. Rapid slip along the central Altyn Tagh Fault: Morphochronologic evidence from Charchen He and Sulamu Tagh. *J. Geophys. Res.* 109, B06401. doi:10.1029/2003JB002558.
- Mériaux, A.S., Tapponnier, P., Ryerson, F.J., Xiwei, X., King, G., Van der Woerd, J., Finkel, R.C., Haibing, L., Caffee, M.W., Zhiqin, X., Wenbin, C., 2005. The Aksay segment of the northern Altyn Tagh fault: Tectonic geomorphology, landscape evolution, and Holocene slip rate. *J. Geophys. Res.* 110, B04404. doi:10.1029/2004JB003210.
- Molnar, P., 1988. Continental tectonics in the aftermath of plate tectonics. *Nature* 335 (6186), 131–137.
- Murray, M.H., Segall, P., 2001. Modeling broadscale deformation in northern California and Nevada from plate motions and elastic strain accumulation. *Geophys. Res. Lett.* 28 (22), 4315–4318.
- Okada, Y., 1985. Surface deformation due to shear and tensile faults in a half-space. *Bull. Seismol. Soc. Am.* 75 (4), 1135–1154.
- Prawirodirdjo, L., Bock, Y., 2004. Instantaneous global plate motion model from 12 years of continuous GPS observations. *J. Geophys. Res.* 109, B08405. doi:10.1029/2003JB002944.
- Prawirodirdjo, L., Bock, Y., McCaffrey, R., Genrich, J., Calais, E., Stevens, C., Puntodewo, S.S.O., Subarya, C., Rais, J., Zwick, P., Fauzi, 1997. Geodetic observations of interseismic strain segmentation at the Sumatra subduction zone. *Geophys. Res. Lett.* 24, 2601–2604.
- Pritchard, M.E., Ji, C., Simons, M., 2006. Distribution of slip from 11 $M_w > 6$ earthquakes in the northern Chile subduction zone. *J. Geophys. Res.* 111, B10302. doi:10.1029/2005JB004013.
- Qinghai Bureau of Geology and Mineral Resources of Qinghai Province, 1991. Regional geology of Qinghai Province. Geological Publishing House. in Chinese with English abstract.
- Rateman, N., Cowgill, E., Lin, D., 2007. Variable structural style along the Karakoram fault explained using triple-junction analysis of intersecting faults. *Geosphere* 3 (2), 71–85. doi:10.1130/GES00067.1.
- Savage, J.C., Burford, R.O., 1973. Geodetic determination of relative plate motion in central California. *J. Geophys. Res.* 78 (5), 832–845.
- Savage, J.C., Gan, W.J., Svarc, J.L., 2001. Strain accumulation and rotation in the Eastern California Shear Zone. *J. Geophys. Res.* 106 (B10), 21995–22007.
- Sella, G.F., Dixon, T.H., Mao, A.L., 2002. REVEL: A model for Recent plate velocities from space geodesy. *J. Geophys. Res.* 107 (B4).
- Shen, J., Wang, Y., Song, F., 2003. Characteristics of the active Xiaojiang fault zone in Yunnan, China: a slip boundary for the southeastward escaping Sichuan–Yunnan Block of the Tibetan Plateau. *J. Asian Earth Sci.* 21, 1085–1096. doi:10.1016/S1367-9120(02)00185-2.
- Shen, Z.K., Lu, J.N., Wang, M., Bürgmann, R., 2005. Contemporary crustal deformation around the southeast borderland of the Tibetan Plateau. *J. Geophys. Res.* 110 (B11), B11409. doi:10.1029/2004JB003421.
- Souter, B. J. (1998), Comparisons of geologic models to GPS observations in southern California, PhD. thesis, Massachusetts Institute of Technology, Cambridge, MA.
- Taylor, M., Peltzer, G., 2006. Current slip rates on conjugate strike-slip faults in central Tibet using synthetic aperture radar interferometry. *J. Geophys. Res.* 111, B12402. doi:10.1029/2005JB004014.
- Taylor, M., Yin, A., 2009. Active structures of the Himalayan–Tibetan orogen and their relationships to earthquake distribution, contemporary strain field, and Cenozoic volcanism. *Geosphere* 5 (3), 199–214. doi:10.1130/GES00217.1.
- Thatcher, W.R., 2003. GPS constraints on the kinematics of continental deformation. *Int. Geol. Rev.* 45 (3), 191–212.
- Thatcher, W., 2007. Microplate model for the present-day deformation of Tibet. *J. Geophys. Res.* 112, B01401. doi:10.1029/2005JB004244.
- Thatcher, W., 2009. How the Continents Deform: The Evidence From Tectonic Geodesy. *Annu. Rev. Earth Planet. Sci.* 37, 14.1–14.26. doi:10.1146/annurev.earth.031208.100035.
- Van der Woerd, J., Tapponnier, P., Ryerson, F., Mériaux, A., Meyer, B., Gaudemer, Y., Finkel, R., Caffee, M., Guoguang, Z., Zhiqin, X., 2002. Uniform postglacial slip-rate along the central 600 km of the Kunlun Fault (Tibet), from ^{26}Al , ^{10}Be , and ^{14}C dating of riser offsets, and climatic origin of the regional morphology. *Geophys. J. Int.* 148 (3), 356–388. doi:10.1046/j.1365-246x.2002.01556.x.
- Vigny, C., Socquet, A., Rangin, C., Chamot-Rooke, N., Pubellier, M., Bouin, M.N., Bertrand, G., Becker, M., 2003. Present-day crustal deformation around Sagaing fault, Myanmar. *J. Geophys. Res.* 108 (B11). doi:10.1029/2002JB001999.
- Wallace, K., Yin, G.H., Bilham, R., 2004. Inescapable slow slip on the Altyn Tagh fault. *Geophys. Res. Lett.* 31, L06613. doi:10.1029/2004GL021014.
- Wang, Q., Zhang, P.Z., Freymueller, J.T., Bilham, R., Larson, K.M., Lai, X., You, X.Z., Niu, Z.J., Wu, J.C., Li, Y.X., Liu, J.N., Yang, Z.Q., Chen, Q.Z., 2001. Present-day crustal deformation in China constrained by global positioning system measurements. *Science* 294 (5542), 574–577.
- Wang, S., Wang, E., Fang, X., Fu, B., 2008. Late Cenozoic systematic left-lateral stream deflections along the Ganzi-Yushu Fault, Xianshuihe Fault System, eastern Tibet. *Int. Geol. Rev.* 50, 624–635. doi:10.2747/0020-6814.50.7.624.
- Washburn, Z., Arrowsmith, J.R., Forman, S.L., Cowgill, E., Xiaofeng, W., Yueqiao, Z., Zhengle, C., 2001. Late Holocene earthquake history of the central Altyn Tagh fault, China. *Geology* 29 (11), 1051–1054. doi:10.1130/0091-7613(2001) 029<1051:LHEHOT>2.0.CO;2.
- Wen, X., Xu, X., Zheng, R., Xie, Y., Wan, C., 2003. Average slip-rate and recent large earthquake ruptures along the Garze-Yushu fault. *Sci. China, Ser. D Earth Sci.* 46, 276–288. doi:10.1360/03dz0022.
- Xu, X., Wen, X., Yu, G., Chen, G., Klinger, Y., Hubbard, J., Shaw, J., 2009. Coseismic reverse and oblique-slip surface faulting generated by the 2008 $M_w 7.9$ Wenchuan earthquake, China. *Geology* 37 (6), 515–518. doi:10.1130/G25462A.1.
- Zhang, P.Z., Shen, Z., Wang, M., Gan, W.J., Bürgmann, R., Molnar, P., 2004. Continuous deformation of the Tibetan Plateau from global positioning system data. *Geology* 32 (9), 809–812.